Strain enhanced visible-ultraviolet absorption of blue phosphorene/MoX₂ (X=S,Se) heterolayers

Di Gu[1,2], Xiaoma Tao[1], Hongmei Chen[1], Yifang Ouyang[1,*], Weiling Zhu[2], Peng Qing[3,*], Yong Du[4]

[1]Guangxi Colleges and Universities Key Laboratory of Novel Energy Materials and Related Technology, College of Physical Science and Technology, Guangxi University, Nanning 530004, People's Republic of China.

[2]Department of Physics, School of Science, Guangdong University of Petrochemical Technology, Maoming, Guangdong 525000, People's Republic of China.

[3]Department of Nuclear Engineering and Radiological Science, University of Michigan, Ann Arbor, MI48109, USA

[4]State Key Laboratory of Powder Metallurgy, Central South University, Changsha 410083, People's Republic of China.

[*] E-mail: ouyangyf@gxu.edu.cn(Y.O.) qpeng.org@gmail.com (Q.P.)

With ultrahigh carrier mobility and large band gap, blue phosphorene (bP) is a promising photoelectronics surpassing black phosphorene and could be further improved by heterostacking. Herein, we report on strain-engineering of the electronic band gaps and light absorption of two van der Waals heterostructures bP/MoS$_2$ and bP/MoSe$_2$ via first-principles calculations. Their electronic band structures are sensitive to in-plane strains. It is interesting and beneficial that biaxial compressive strain range of -0.02 to -0.055 induce the direct band gap in bP/MoSe$_2$. There are two critical strains for bP/MoS(Se)$_2$ heterostructures, where the semiconductor-metal transition could be observed. The bP/MoS(Se)$_2$ heterostructures exhibits strong visible-ultraviolet light absorption, which could be further enhanced via biaxial strain. Our results suggest that bP/MoS(Se)$_2$ heterostructures have promising electronics and visible-ultraviolet optoelectronic applications.

1. Introduction

Graphene, as a two-dimensional (2D) atomically thin material, has attracted a great of attention since its discovery in 2004[1]. Unlike a general semiconductor, graphene has no gap between its valence and conduction bands, which limits its electronic applications [2, 3]. As alternatives of graphene, the transition metal

2

dichalcogenides (TMDs), such as MoS_2 and $MoSe_2$, were reported that they had sizable bandgap, advantageous optoelectronic and distinguished mechanical properties[4-7]. Especially, both of monolayer MoS_2 and $MoSe_2$ are of direct band gap which is suitable for electronic or optoelectronic applications[5, 8-10]. Phosphorus was reported as another class of 2D material beyond graphene and transition metal dichalcogenides [11-14]. The transport properties of black phosphorus are prominent[15]. For example, the electron carrier mobility of monolayer black phosphorus is high up to 1000 cm^2/Vs [12], which is higher than the electron carrier mobility of semimetallic graphene and monolayer MoS_2 (10-200 cm^2/Vs). Similar to black phosphorus, blue phosphorene (bP), which could be converted from the black phosphorene by certain dislocation of constituent P atoms, is another allotrope of phosphorene [13, 16-19]. Recently, bP was predicted by the theoretical calculations with a higher hole mobility about 1800 cm^2/Vs and a larger bandgap of ~ 2.0 eV than black phosphorene [16, 19, 20].

Due to the fact that the application of the 2D material was limited by single material system with restricted properties, many researchers tried to vertically stack two different 2D materials to achieve van der Waals (vdW) heterostructures via vdW interaction[21-23]. Recent studies have shown that vdW heterostructures would be a facile way to achieve advanced properties by combination of different monolayers 2D materials[24-29]. For example, Deng *et al.* reported that a gate-tunable P-N diode based on a P-type black phosphorus and a N-type monolayer MoS_2 as a photodetector,

3

which showed a photodetection responsivity of 418 mA/W and was much higher than the value of 4.8 mA/W for the single black phosphorus phototransistors [30]. Ganesan *et al.* demonstrated theoretically that phosphorene and TMDs heterostructures would be suitable for excitonic thin film solar cell applications [31]. The black phosphorus and MoS_2 vdW heterostructure possessed good piezoelectric effect via the compressive strain [32]. Moreover, it was worth to note that bP shared a similar hexagonal crystal structure and nearly identical lattice constants with MoS_2 and $MoSe_2$. From the point view of lattice match, bP would be more feasible to stack vdW heterostructures with MoS_2 and $MoSe_2$ than black phosphorene. Therefore, it is thus interesting to investigate the electronic and optical properties of $bP/MoS(Se)_2$ vdW heterostructures.

In this work, the equilibrium geometry of the stable $bP/MoS(Se)_2$ vdW heterostructures was constructed, and then the effect of different strain on the electronic and optical properties of $bP/MoS(Se)_2$ vdW heterostructures were investigated by using density functional theory (DFT).

2. Results

In order to construct stable hybrid $bP/MoS(Se)_2$ vdW heterostructures, monolayer MoS_2, $MoSe_2$ and bP were relaxed firstly, and the values of lattice constants were respectively 3.169Å, 3.319Å and 3.278Å, which were in consistent

4

with the previous reported data[9, 15]. Six possible stacking configurations of bP/MoS(Se)$_2$ vdW heterostructures, as shown in Figure 1(a)–1(f) namely A1-, A2-, A3-, B1-, B2- and B3-stacking, were considered. For the A1-stacking, the top layer bP was directly stacked on the bottom layer MoS$_2$ or MoSe$_2$, where the underneath P atom was just above the S or Se atom, and the three other upper P atoms were just located in the center of the adjacent three puckered hexagon of the bottom layers MoS(Se)$_2$ respectively. The A2-stacking and the A3-stacking could be viewed as that the top layer bP of the A1-stacking was kept fixed, and the bottom layer MoS(Se)$_2$ of the A1-stacking was shifted along the armchair direction by 1/3 or 2/3 length of the cell, respectively. As a result, for the A2-stacking, the underneath P atom was just above the Mo atom and the upper P atoms were just above the S or Se atoms, where the edge of the puckered hexagon of the bottom layer MoS(Se)$_2$ and the edge of the puckered hexagon of the top layer bP were overlapping nicely. For the A3-stacking, the underneath P atom was just located in the center of the puckered hexagon of the bottom layer MoS(Se)$_2$, and the three other upper P atoms were just above the Mo atoms. For the B1-, B2- and B3-stacking, the MoS(Se)$_2$ were along opposite direction. Analogously, the B2-stacking and the B3-stacking could be viewed as the bottom layer MoS(Se)$_2$ of the B1-stacking was shifted along the armchair direction by 1/3 or 2/3 length of the cell, respectively. Moreover, the B1-, B2- and B2-stacking could also be viewed as that the bottom layer MoS(Se)$_2$ were rotated 180 degrees from A3-, A1- and A2-stacking respectively. All of the six stacking configurations were fully relaxed

5

for getting stable atomic configuration.

The Energy difference ΔE_i (eV) is the difference between the energies of optimized bP/MoS(Se)$_2$ heterostructures and the most stable heterostructure (A2). As shown in Figure 1(g), the trends of ΔE_i between bP/MoS$_2$ and bP/MoSe$_2$ vdW heterostructures are very similar, especially both the ΔE_i of B2-stackings were the largest, while those of the A2-stackings were the lowest. This indicates that the most stable structure is A2-stacking. As shown in Figure 1(h), the A2-stackings were chosen as the optimum stacking order in the bP/MoS(Se)$_2$ vdW heterostructures. The interlayer distance (d) of the bP/MoS(Se)$_2$ were estimated to be about 3.11(3.20)Å, which were in consistent with the previous reported data of vdW heterostructures [33]. The calculated optimal lattice parameters of bP/MoS$_2$ and bP/MoSe$_2$ vdW heterostructure were 3.223 Å and 3.298 Å, respectively. Compared with the lattice parameters of monolayer MoS(Se)$_2$ and monolayer bP, the lattice mismatches for bP/MoS$_2$ and bP/MoSe$_2$ vdW heterostructures were about 3.32% and 1.24% respectively, both of them were in an acceptable range.
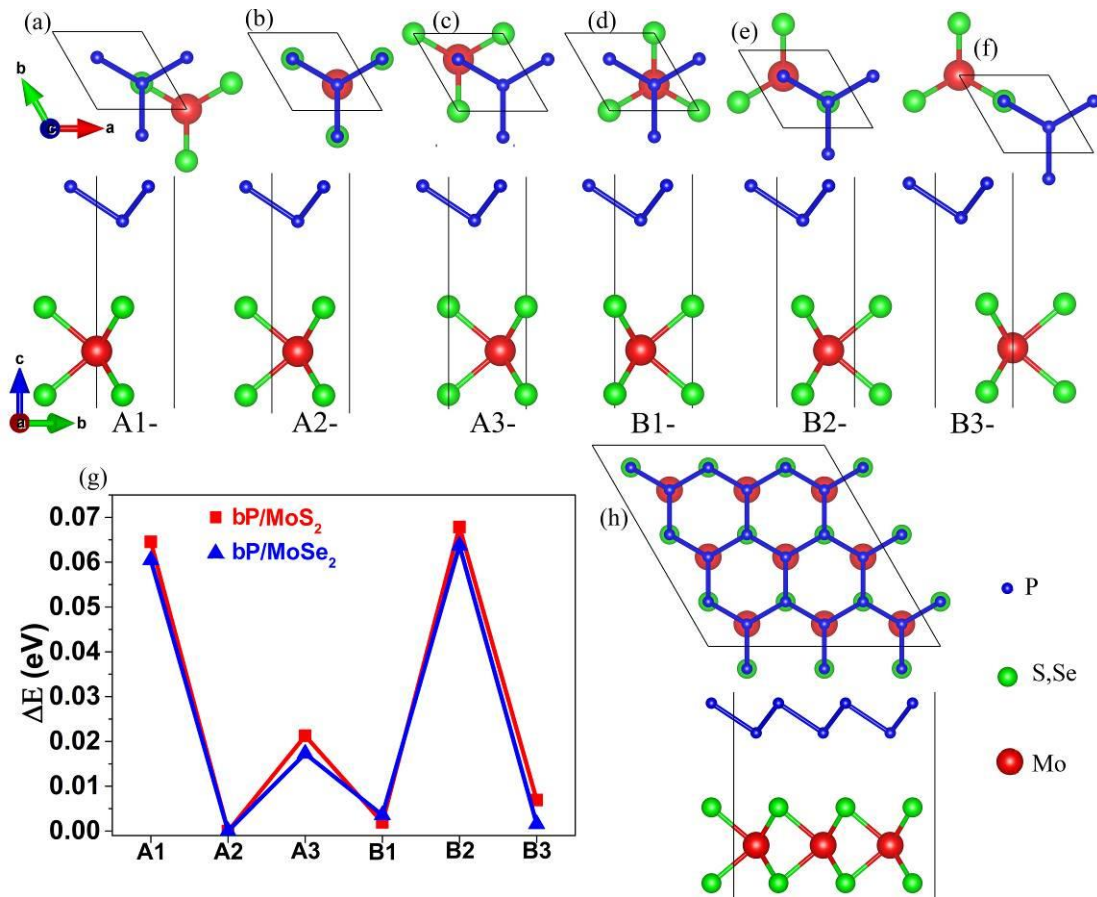
Figure 1. Six stacking structures of bP/MoS(Se)$_2$ heterostructures, (a)–(f) top and side views of A1-, A2-, A3-, B1-, B2- and B3- stacking. (g) Energy difference ΔE_i (eV) between the energies of optimized bP/MoS(Se)$_2$ heterostructures and the most stable heterostructure (A2)**.** (h) Top and side views of the optimum stacking (A2-) order of the bP/MoS(Se)$_2$ heterostructures.

The electronic band structures of bP monolayer, MoS$_2$ monolayer, MoSe$_2$ monolayer, bP/MoS$_2$ and bP/MoS$_2$ vdW heterostructures were shown in Figure 2 (HSE06 method) and Figure S1 (PBE method). Due to the improper treatment of the

7

Coulomb repulsion, the band gaps from the GGA-PBE functionals are underestimated. In comparison, the band gaps based on the hybrid HSE06 method are enhanced. Except for the bigger band gaps, the electronic band structures based on HSE06 method computation are similar to those based on PBE method computation. As shown in Figure 2(b), bP monolayer was an indirect gap semiconductor with Eg of ~ 2.778 eV. The valence band maximum (VBM) located between K and $\varGamma$ points and the conduction band minimum (CBM) located between the $\varGamma$ and M points. It was seen from Figure 2(c) and Figure 2(d) that both MoS_2 and $MoSe_2$ monolayer were a direct gap semiconductor with Eg of ~2.208 eV and 1.889 eV respectively. Their VBMs and CBMs both located at the K point. The calculated electronic band structures of monolayer MoS_2, $MoSe_2$ and bP all agreed well with previous works [9, 15]. As shown in Figure 2(e) and Figure 2(f), the bP/MoS(Se)$_2$ vdW heterostructures, indirect gap semiconductor could be found, because of the band structures preserved both the properties of bP and MoS(Se)$_2$. The Eg of bP/MoS$_2$ and bP/MoSe$_2$ vdW heterostructures were 1.677 eV and 1.769 eV, respectively. For the bP/MoS$_2$ vdW heterostructure, the VBM located at the $\varGamma$ point but the CBM located at the K point. For the bP/MoSe$_2$ vdW heterostructure, the VBM located at the K point, while the CBM located between the $\varGamma$ and M points. What is more, the energy level of VBM at $\varGamma$ point and K point were almost the same.
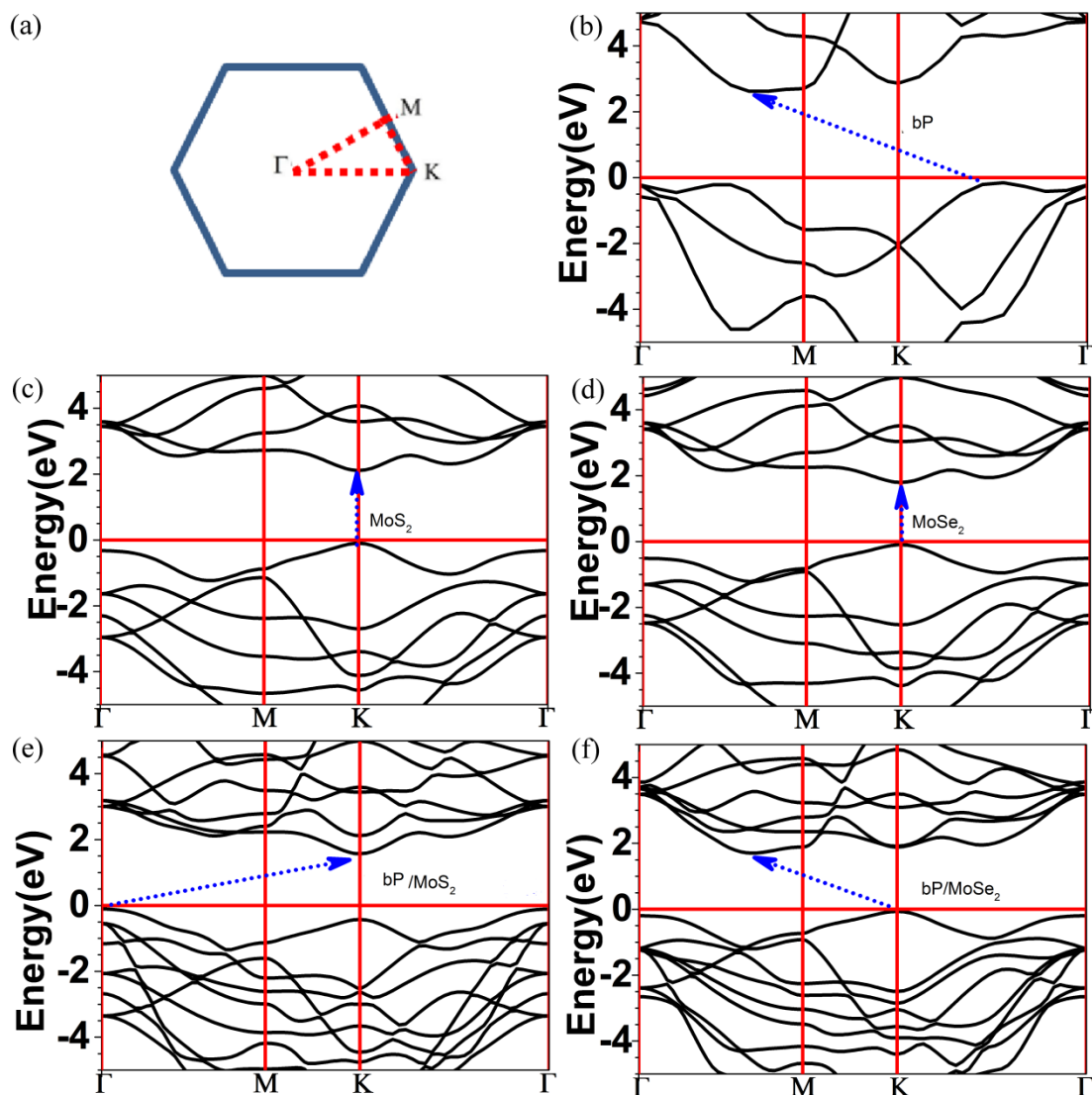
(a)

(b)

(c)

(d)

(e)

(f)

Figure 2. (a) Brillouin zone with high-symmetry points labeled. Band structures （HSE06） of (b) bP monolayer, (c) MoS_2 monolayer, (d) $MoSe_2$ monolayer, (e) bP/MoS_2 vdW heterostructure and (f) bP/$MoSe_2$ vdW heterostructure.

The planar average potential was shown in Figure 3 and Figure S2 in Supplementary Information. The energy of a stationary electron in the vacuum nearby

the surface (E_{vac}) of MoS_2, $MoSe_2$, bP, bP/MoS_2 and bP/$MoSe_2$ were 2.459 eV, 2.258

eV, 1.807 eV, 5.034 eV and 4.786 eV, respectively. The depth of electrostatic potential,

from E_{vac} to the minimum of planar average potential, was 20.187 eV, 15.317 eV and

19.747 eV for MoS_2, $MoSe_2$ and bP, respectively. The depth of the MoS_2 was close to

the depth of bP. On the contrary, the difference between $MoSe_2$ and bP was obvious.

These difference between MoS_2 ($MoSe_2$) and bP would lead to a similar conclusion in

the potential drop. For the bP/MoS_2 vdW heterostructure, the potential drop was about

0.839 eV (Figure 3(a)) and the planar-averaged differential charge density across

bP/MoS_2 slightly changed (Figure 3(b)). As shown in Figure 3(c), the decomposed

charge density of the VBM and CBM of bP/MoS_2 vdW heterostructure indicated that

Mo atom mainly contribute to the VBM and CBM. And the calculated band

alignments of bP/MoS_2 vdW heterostructure was shown in Figure 3(d), indicating a

type-I alignment. For the bP/$MoSe_2$ vdW heterostructure, the potential drop across

bP/$MoSe_2$ was 4.208 eV (Figure 3(e)). A large potential difference for bP/$MoSe_2$

indicated that a large intrinsic electric field across the interface, where the electrons

and holes were more easily separated or transferred. The decomposed charge density

of the VBM and CBM of bP/MoS_2 vdW heterostructure indicated that Mo atom

contributed to the VBM and P atom mainly contributed to the CBM, respectively

(Figure 3(g)). As seen in Figure 3(h), the band edge positions of these vdW

heterostructures were located between CBM of bP and VBM of $MoSe_2$ indicating a

type-II heterostructure, which was important for application in photovoltaics and
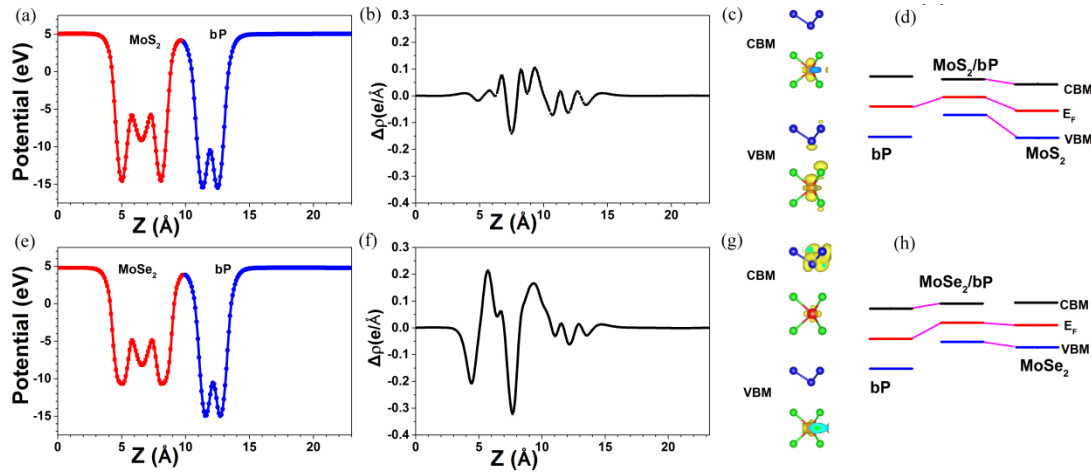
10

photodetection.

Figure 3. (a)(e) The planar average potential, (b)(f) the planar-averaged differential charge density, (c)(g) the band decomposed charge density of the CBM and VBM and (d)(h) the Band alignments of bP/MoS$_2$ and bP/MoSe$_2$ vdW heterostructure, respectively

In-plane uniaxial strain and biaxial strain on the bP/MoS(Se)$_2$ vdW heterostructures were applied by changing the lattice parameters. Here, "-" represents compression and "+" represents stretching. As seen in Figure 4(a) and Figure 3S (a), the band gap values of the bP/MoS$_2$ vdW heterostructures were sensitive to the biaxial strain or uniaxial strain. The band gap values computed from HSE06 functionals are bigger than those from PBE functionals. However, the trends of the change of the band gaps of bP/MoS2 vdW heterostructure in responding to the strain are concordant for both methods. Therefore, the band gaps predicted from HSE06 functionals were taken

11

for example to analyze the trend of bP/MoS$_2$ vdW heterostructure as a function of biaxial strain. The band gap linearly decreased from 1.677 eV to 0.113 eV when the biaxial strain increased from 0 to +8%. When the biaxial strain was +10%, the band gap value was less than zero, which indicated bP/MoS$_2$ heterostructure had transferred from semiconductor to typically metallic and the transferred stretching strain is about 9%.

Moreover, when the biaxial strain decreased to -2%, the band gap reached the maximum ~ 2.149 eV. It was worth noting that under the state of biaxial strain -2%, the lattice constants of bP/MoS$_2$ heterostructure was 3.159 Å closely to the lattice constants of the monolayer MoS$_2$ (3.169 Å). The band gap linearly decreased as the decrease of the biaxial strain from -2% to -10%. Especially, when the biaxial strain was -10%, the band gap value was less than zero, too, which indicated bP/MoS$_2$ heterostructure could also transfer from semiconductor to typically metallic under the compression and the transferred compressing strain is about -8.5%. The Figure 4(b) shown that the conduction and valance band energies in the first Brillouin zone of bP/MoS$_2$ vdW heterostructure as functions of applied biaxial strain. All points except Γ_{VBM} possessed similar trend. The energy value of those symmetric points increased as the increase of biaxial strain from -10% to -2%. When the biaxial strain was -2%, they possessed the maximum value, and then they decreased as the increase of biaxial strain from -2% to 8%. The change of Γ_{VBM} wasn't obvious when the biaxial strain varied. It was worth noting that K_{CBM} was the minimum among the symmetric points of CBM and Γ_{VBM}

12

was the maximum among the symmetric points of VBM indicating that the relative position of VBM and CBM were not changed. Moreover, when the biaxial strain was ±10%, the K_{CBM} was less than Fermi energy and the Γ_{VBM} was slightly higher than Fermi energy level, which indicated bP/MoS$_2$ heterostructure had transferred from semiconductor to metallic. The detailed band structures (HSE06 and PBE) and projected densities of states (PBE) of the bP/MoS$_2$ vdW heterostructures at different biaxial strain were presented in Figure S4 in Supplementary Information. The details of band structures agreed well with the analysis above, especially the transformation from semiconductor to metallic was obvious. From the PDOS of the bP/MoS$_2$ vdW heterostructures, we could clearly see that when biaxial strain was 0%, it was p-orbitals of Mo and s-orbitals of S and P that contributed mainly to the VBM below Fermi level, while above the Fermi level, p-orbitals of Mo and s-orbitals of S contributed mainly to the CBM, indicating that bP/MoS$_2$ was a type-I heterostructure which coincided with the analysis of the band decomposed charge density and Band alignments mentioned above. When the biaxial strain was +8%, the p-orbitals of Mo shifted to Fermi level, while the biaxial strain was -8%, it was the s-orbitals of P that shifted to Fermi level obviously, which was the important reason for the emergence of metallic.

Similar to the bP/MoS$_2$ vdW heterostructures, the band gaps of bP/MoSe$_2$ vdW heterostructures could be widely tuned through uniaxial strain or biaxial strain. Specially, beyond a critical biaxial strain -12% or +14%, the transition from

semiconductor to metal could be observed clearly (Figure 4(c)) and the transferred stretching and compressing strain are -10.5% and 13%, respectively. Under the state of biaxial strain -1%, the lattice constants of bP/MoSe$_2$ heterostructure was 3.265 Å closely to the lattice constants of the monolayer bP (3.278 Å), in this case, the band gap of bP/MoSe$_2$ vdW heterostructure reached the maximum value. What was more important, in the strain of -2% ~ -5.5% range, the system exhibits a direct band gap character, the VBM and CBM both located at the K point. More details were shown in the conduction and valance band energies of the six points (Γ_{VBM}, M_{VBM}, K_{VBM}, Γ_{CBM}, M_{CBM} and K_{CBM}) as functions of applied biaxial strain. As shown in Figure 4(d), within the strain range of 0%~10%, all points except Γ_{VBM} reduced as the biaxial strain increased, yet the Γ_{VBM} was stable without obvious change. The change in the 0%~-6% was more complicated and important. It was worth noting that when the biaxial strain was 0%, M_{CBM} was the manimum and K_{CBM} was just slightly larger than M_{CBM}, while the biaxial strain was in the range of -2%~-10%, the K_{CBM} dramatically reduced to be the minimum. On the contrast, the K_{VBM} kept stable without obvious change to be the maximum during the -2%~-5.5% range. So the system exhibits a direct band gap in the range of -2%~-5.5%. Moreover, when the biaxial strain was -12% or +14% the K_{CBM} was less than Fermi energy level and the Γ_{VBM} was slightly higher than Fermi energy level, which indicated bP/MoSe$_2$ heterostructure had changed from semiconductor to typically metallic. The detailed band structures (HSE06 and PBE) and projected densities of states (PBE) of the bP/MoSe$_2$ vdW heterostructures at

14

different biaxial strain were presented in Figure S5 in Supplementary Information. From the band structures of the bP/MoSe$_2$ vdW heterostructures, the change of the conduction and valance band energies of the six points could be observed clearly, especially an intriguing transition from indirect to direct and from semiconductor to metal. From the PDOS of the bP/MoSe$_2$ vdW heterostructures, we could clearly see that when biaxial strain was 0%, it was *p*-orbitals of Mo and *s*-orbitals of Se and P that contributed mostly to the VBM below Fermi level, while above the Fermi level, *p*-orbitals of Mo and *s*-orbitals of Se contributed mostly to the CBM, indicating that bP/MoSe$_2$ was a type-II heterostructure which was useful photovoltaic devices and photocatalytic due to the desirable characteristic of efficient electron-hole separation. As biaxial strain increased, the orbitals of CBM, including *p*-orbitals of Mo and *s*-orbitals of Se, gravitated to Fermi level and the band gap reduced progressively. At +10% biaxial strain, the orbitals of CBM across Fermi level leaded to the change from semiconductor to metallic. Within the 0%~-2% range of biaxial strain, the orbitals of CBM kept away from the Fermi level, which coincided with the enlargement of band gap. As biaxial strain decreased from -2% to -10%, *p*-orbitals of P, which contributed mostly to the CBM, gravitated to Fermi level and the band gap reduced progressively. At -10% biaxial strain, the orbitals of CBM across Fermi level leaded to the change from semiconductor to metallic. Therefore, theoretical predictions suggest that the bP/MoSe$_2$ vdW heterostructures are very promising for optoelectronic applications due to their tunable band gaps by applying strain.
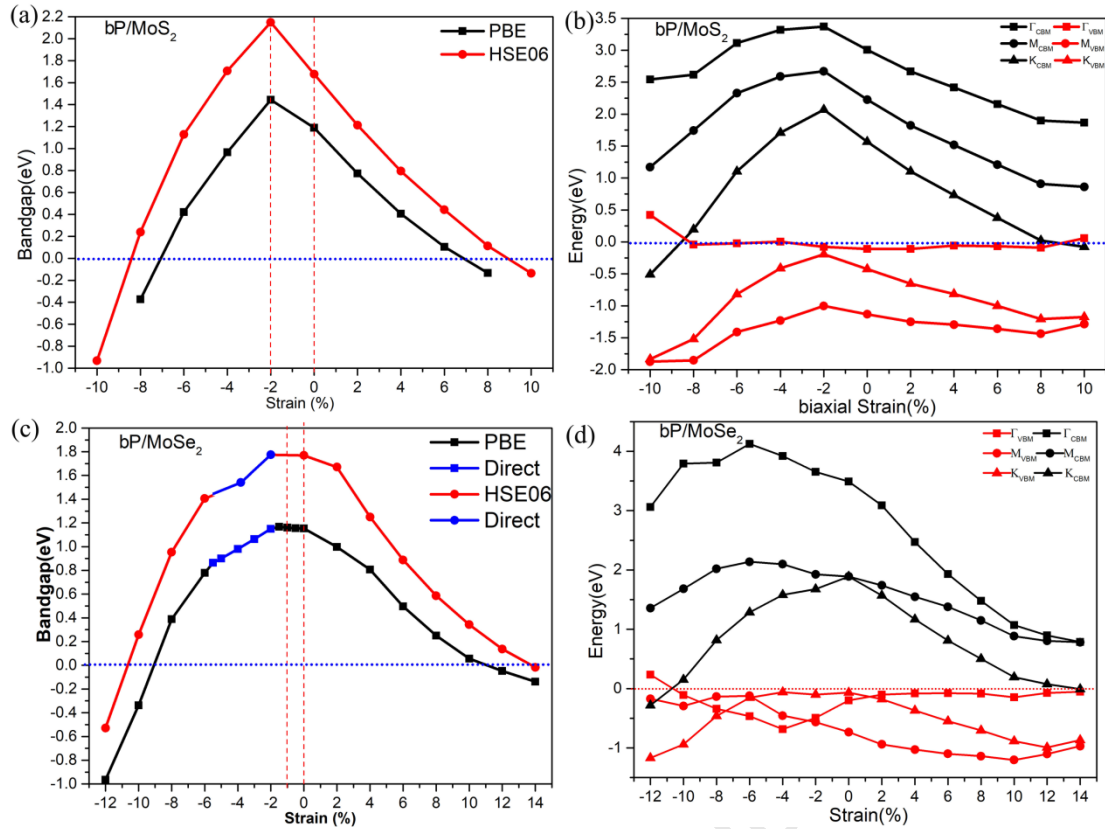
15

Figure 4. (a) The band gap (HSE06 and PBE) of bP/MoS$_2$ vdW heterostructure as a function of biaxial strain. (b) The conduction and valance band energies (HSE06) at different symmetry point in the first Brillouin zone of bP/MoS$_2$ vdW heterostructure as a function of biaxial strain. (c) The band gap (HSE06 and PBE) of bP/MoSe$_2$ vdW heterostructure as a function of biaxial strain. (d) The conduction and valance band energies (HSE06) at different symmetry point in the first Brillouin zone of bP/MoSe$_2$ vdW heterostructure as a function of biaxial strain.

The absorption coefficient was an important factor for photoelectronic devices and solar cells. The perfect devices should absorb visible light and UV light as much

16

as possible. However, the previous paper reported that $MoS(Se)_2$ single layer exhibited light absorption mainly in the visible light region, while the bP single layer exhibited light absorption only in the UV light region [34]. As shown in the Figure 5 $bP/MoS(Se)_2$ heterostructures exhibits strong visible-UV light absorption in the wavelength range of 50 to 800 nm, especially the 60-300 nm, indicating that $bP/MoS(Se)_2$ heterostructures could break the limitation of a single layer and combine together the advantageous properties of different layers. The reasons for this optical absorption phenomenon vdW heterostructures were understandable, including that the interlayer coupling, the electronic states overlapping and charge transfer in the heterostructures, where the new optical transitions were induced [35]. This interesting phenomenon was also found in the black (blue) phosphorus/g-ZnO vdW heterostructures [35]. In addition, the absorption coefficients of $bP/MoS(Se)_2$ heterostructures about 10^5 cm^{-1} to 10^6 cm^{-1} under visible-UV light, which are stronger than that of black(blue)-P/g-ZnO heterojunction (about 10^4 cm^{-1})[35], are similar to the absorption coefficients of InSe/SnS and InSe/GeSe heterojunctions[36]. Furthermore, as shown in Figure 5(a) and 5(c), red shift has taken place at its absorption edge as the biaxial strain increased. While the absorption coefficients increased as the biaxial strain decreased. From the insets of Figure S6, the relationship between absorption edge, optical energy gap and biaxial strain were obvious, especially the optical energy gap were sensitive to the biaxial strain. The optical energy gap change curves coincided with the band gap of $bP/MoS(Se)_2$ vdW heterostructure as a function of

17

strain mentioned above, indicating that it was effective to tune the optical properties of bP/MoS(Se)$_2$ vdW heterostructures via biaxial strain, therefore, these theoretical predictions suggest that bP/MoS(Se)$_2$ heterostructures are promising visible-ultraviolet optoelectronic applications due to their tunable electronic and optical properties.
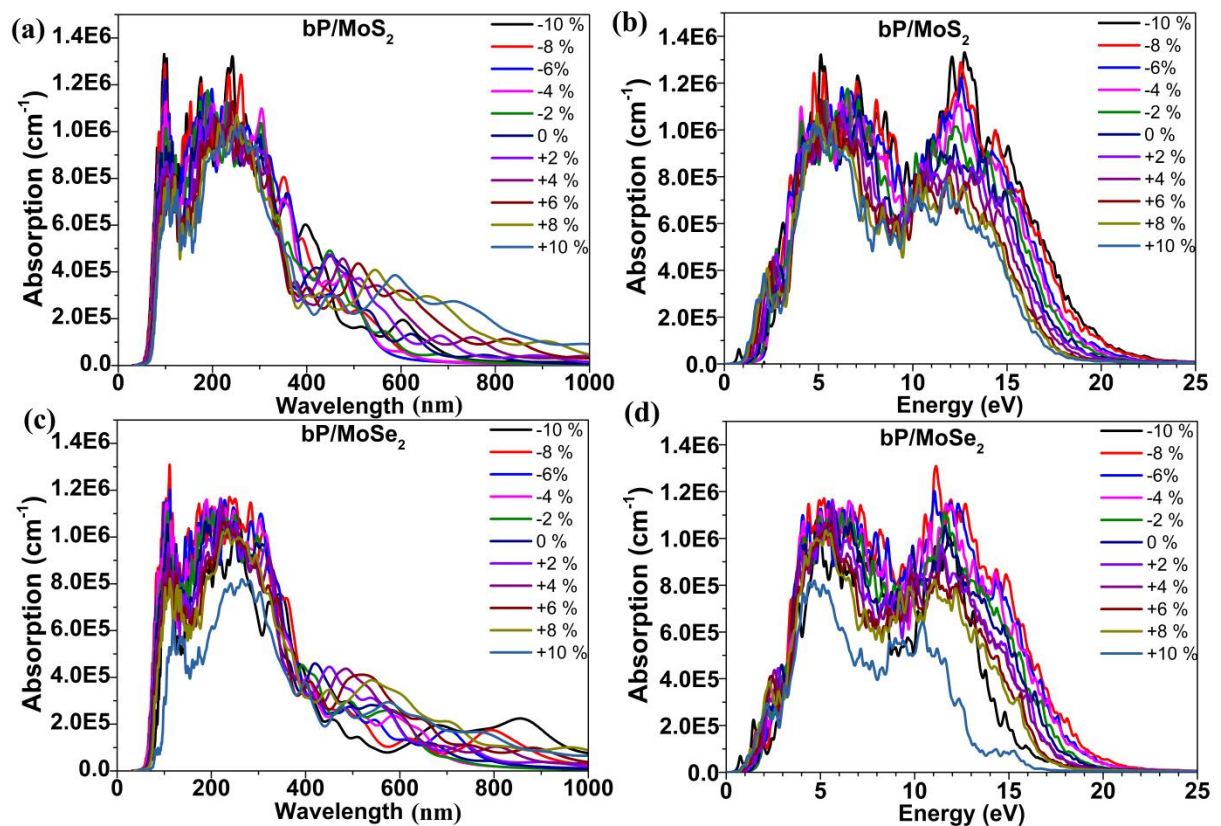

Figure 5. Absorption coefficients of (a)(b) bP/MoS$_2$ and (c)(d) bP/MoSe$_2$. (a)(c) and (b)(d) were absorption coefficient versus wavelength and energy, respectively.

3. Conclusion

In conclusion, the strain-engineering of the structural, energetic, electronic and

optical properties of the $bP/MoS(Se)_2$ heterostructures have been performed by means of high-fidelity first-principles calculations, including uniaxial strain and biaxial strains. The $bP/MoS(Se)_2$ vdW heterostructures exhibited indirect gap characteristics. The band gap values were sensitive to the in-plane strain. Specially, for $bP/MoSe_2$ heterostructure system, biaxial compressive strain range of -2% to -5.5% could induce the modulation of direct band gap character with the VBM and CBM both located at the K point. However, bP/MoS_2 heterostructures do not exhibit a direct band gap under uniaxial strain. What is more, there are two critical strains of -0.085(-0.105) and +0.09(+0.135) for $bP/MoS(Se)_2$ heterostructures, where the semiconductor-metal transition could be observed. Moreover, the $bP/MoS(Se)_2$ heterostructures exhibited strong visible-UV light absorption in the wavelength range of 50 to 800 nm, and it was effective to tune and enhance the optical properties of $bP/MoS(Se)_2$ vdW heterostructures via biaxial strain. Therefore, these theoretical predictions suggest that $bP/MoS(Se)_2$ heterostructures are promising excellent visible-ultraviolet optoelectronic applications due to their tunable electronic and optical properties.

4. Methods

The present calculations were performed using the Vienna ab initio simulation package (VASP) [37] in conjunction with the projector-augmented-wave (PAW) potential [38]. The Perdew-Burke-Ernzerhof (PBE) functional of the generalized

19

gradient approximation (GGA) was used to describe the exchange-correlation energy

[39]. The HSE06 hybrid functional[40] was adopted to calculate more accurate band

gaps. In order to better take into account the vdW forces between monolayer

$MoS(Se)_2$ and monolayer bP, the van der Waals density functional of optB88 [41-43]

was considered in all calculations to give an improved description for $bP/MoS(Se)_2$

vdW heterostructures. The energy cutoff for the plane-wave expansion of the wave

function was set to 400 eV. All the structures were fully relaxed until satisfying an

energy convergence of 10^{-4} eV and the maximum Hellmann Feynman force

convergence of 0.01 eV/Å. The Gamma center scheme was used for the first Brillouin

zone integration with a fine grid of $9 \times 9 \times 1$ and $12 \times 12 \times 1$ for structure optimization and

static calculation [44], respectively. The thickness of the vacuum region along the z

direction was more than 15 Å to eliminate the artificial interactions due to the periodic

image.

Supporting Information.

Supplementary Figures of Figure S1-S6 for electronic band structures, planar average

potentials, PBE bandgap tuning, Band structures at -10, -2, 0, 10%, and absorption

coefficients of $bP/MoS(Se)_2$, respectively.

AUTHOR INFORMATION

Corresponding Author

COMPETING INTERESTS

The authors declare no competing financial interest.

ACKNOWLEDGMENTS

DATA AVAILABILITY

All data generated or analyzed during this study are included in this published article and its supplementary information files.

Author contributions

Y.O., and Q.P. designed the project. D.G., X.T., H.C., and W.Z. carried out the simulations. D.G., X.T., Y.D. and Y.O. done the analysis. Y.O., and Q.P. wrote the paper. All authors discussed and commented on the manuscript.

21

References

[1] K.S. Novoselov, A.K. Geim, S.V. Morozov, D. Jiang, Y. Zhang, S.V. Dubonos, I.V. Grigorieva, A.A. Firsov, *Science*, **2004**, 306, 666-669.

[2] K.S. Novoselov, *Angew. Chem. Int. Ed.*, **2011**, 50, 6986-7002.

[3] Q. Peng, S. De, *Phys. E (Amsterdam, Neth.)*, **2012**, 44, 1662-1666.

[4] Y.G. Li, Y.L. Li, C.M. Araujo, W. Luo, R. Ahuja, *Catal. Sci. Technol.*, **2013**, 3, 2214-2220.

[5] K.F. Mak, C. Lee, J. Hone, J. Shan, T.F. Heinz, *Phys. Rev. Lett.*, **2010**, 105, 136805.

[6] Q. Peng, S. De, *Phys. Chem. Chem. Phys.*, **2013**, 15, 19427.

[7] Q.H. Wang, K. Kalantar-Zadeh, A. Kis, J.N. Coleman, M.S. Strano, *Nat. Nanotechnol.*, **2012**, 7, 699-712.

[8] S. Lebègue, O. Eriksson, *Phys. Rev. B*, **2009**, 79, 115409.

[9] Y. Ding, Y. Wang, J. Ni, L. Shi, S. Shi, W. Tang, *Phys. B (Amsterdam, Neth.)*, **2011**, 406, 2254-2260.

[10] T. Korn, S. Heydrich, M. Hirmer, J. Schmutzler, C. Schüller, *Appl. Phys. Lett.*, **2011**, 99, 102109.

[11] H. Liu, A.T. Neal, Z. Zhu, Z. Luo, X. Xu, D. Tomanek, P.D. Ye, *ACS Nano*, **2014**, 8, 4033-4041.

[12] E.S. Reich, *Nature*, **2014**, 506, 19.

[13] Z. Zhu, D. Tomanek, *Phys. Rev. Lett.*, **2014**, 112, 176802.

[14] C. Wang, Q. He, U. Halim, Y. Liu, E. Zhu, Z. Lin, H. Xiao, X. Duan, Z. Feng, R. Cheng, N.O. Weiss, G. Ye, Y.C. Huang, H. Wu, H.C. Cheng, I. Shakir, L. Liao, X. Chen, W.A. Goddard Iii, Y. Huang, X. Duan, *Nature*, **2018**, 555, 231-236.

[15] X. Zhu, T. Zhang, D. Jiang, H. Duan, Z. Sun, M. Zhang, H. Jin, R. Guan, Y. Liu, M. Chen, H. Ji, P. Du, W. Yan, S. Wei, Y. Lu, S. Yang, *Nat. Commun.*, **2018**, 9, 4177.

[16] B. Ghosh, S. Nahas, S. Bhowmick, A. Agarwal, *Phys. Rev. B*, **2015**, 91, 115433.

[17] J.L. Zhang, S. Zhao, C. Han, Z. Wang, S. Zhong, S. Sun, R. Guo, X. Zhou, C.D. Gu, K.D. Yuan, Z. Li, W. Chen, *Nano Lett.*, **2016**, 16, 4903-4908.

[18] D. Tristant, A. Cupo, V. Meunier, *2D Mater.*, **2018**, 5, 035044.

[19] J. Zhuang, C. Liu, Q. Gao, Y. Liu, H. Feng, X. Xu, J. Wang, J. Zhao, S.X. Dou, Z. Hu, Y. Du, *ACS Nano*, **2018**, 12, 5059-5065.

[20] J. Xiao, M. Long, X. Zhang, J. Ouyang, H. Xu, Y. Gao, *Sci. Rep.*, **2015**, 5, 9961.

[21] A.K. Geim, I.V. Grigorieva, *Nature*, **2013**, 499, 419-425.

[22] Q. Li, J. Yang, L. Zhang, *J. Phys. Chem. C*, **2018**, 122, 18294-18303.

[23] S. Wang, C. Ren, H. Tian, J. Yu, M. Sun, *Phys. Chem. Chem. Phys.*, **2018**, 20, 13394-13399.

[24] V.O. Ozcelik, J.G. Azadani, C. Yang, S.J. Koester, T. Low, *Phys. Rev. B*, **2016**, 94, 035125.

[25] Z. Guo, N. Miao, J. Zhou, B. Sa, Z. Sun, *J. Mater. Chem. C*, **2017**, 5, 978-984.

[26] Y.C. Huang, X. Chen, C. Wang, L. Peng, Q. Qian, S.F. Wang, *Nanoscale*, **2017**, 9, 8616-8622.

[27] W. Li, T. Wang, X. Dai, Y. Ma, Y. Tang, *J. Alloys Compd.*, **2017**, 705, 486-491.

[28] Q. Yang, C.-J. Tan, R.-S. Meng, J.-K. Jiang, Q.-H. Liang, X. Sun, D.-G. Yang, X.-P. Chen, *IEEE Electron Device Lett.*, **2017**, 38, 145-148.

[29] W.C. Yap, Z. Yang, M. Mehboudi, J.-A. Yan, S. Barraza-Lopez, W. Zhu, *Nano Res.*, **2017**, 11, 420-430.

[30] Y. Deng, Z. Luo, N.J. Conrad, H. Liu, Y. Gong, S. Najmaei, P.M. Ajayan, J. Lou, X. Xu, P.D. Ye, *ACS Nano*, **2014**, 8, 8292-8299.

[31] V.D.S.O. Ganesan, J. Linghu, C. Zhang, Y.P. Feng, S. Lei, *Appl. Phys. Lett.*, **2016**, 108, 122105.

[32] L. Huang, Y. Li, Z. Wei, J. Li, *Sci. Rep.*, **2015**, 5, 16448.

[33] Z.Y. Zhang, M.S. Si, S.L. Peng, F. Zhang, Y.H. Wang, D.S. Xue, *J. Solid State Chem.*, **2015**, 231, 64-69.

[34] Q. Peng, Z. Wang, B. Sa, B. Wu, Z. Sun, *Sci. Rep.*, **2016**, 6, 31994.

[35] W. Zhang, L. Zhang, *RSC Adv.*, **2017**, 7, 34584-34590.

[36] C.-x. Xia, J. Du, X.-w. Huang, W.-b. Xiao, W.-q. Xiong, T.-x. Wang, Z.-m. Wei, Y. Jia, J.-j. Shi, J.-b. Li, *Phys. Rev. B*, **2018**, 97, 115416.

[37] G. Kresse, J. Furthmüller, *Phys. Rev. B*, **1996**, 54, 11169-11186.

[38] P.E. Blochl, *Phys. Rev. B: Condens. Matter*, **1994**, 50, 17953-17979.

[39] J.P. Perdew, K. Burke, M. Ernzerhof, *Phys. Rev. Lett.*, **1996**, 77, 3865-3868.

[40] J. Paier, M. Marsman, K. Hummer, G. Kresse, I.C. Gerber, J.G. Angyan, *J. Chem. Phys.*, **2006**, 124, 154709.

[41] A.D. Becke, *Phys. Rev. A: Gen. Phys.*, **1988**, 38, 3098-3100.

[42] J. Klimes, D.R. Bowler, A. Michaelides, *J. Phys.: Condens. Matter*, **2010**, 22, 022201.

[43] J. Klimeš, D.R. Bowler, A. Michaelides, *Phys. Rev. B*, **2011**, 83, 195131.

[44] H.J. Monkhorst, J.D. Pack, *Phys. Rev. B*, **1976**, 13, 5188-5192.